PAPER • OPEN ACCESS

Simulation of DIII-D disruption with argon pellet injection and runaway electron beam

To cite this article: C. Zhao *et al* 2024 *Nucl. Fusion* **64** 126026

OPEN ACCESS
IOP Publishing | International Atomic Energy Agency
Nuclear Fusion
Nucl. Fusion 64 (2024) 126026 (9pp)
https://doi.org/10.1088/1741-4326/ad80ab

Simulation of DIII-D disruption with argon pellet injection and runaway electron beam

C. Zhao[1,*], C. Liu[2], S.C. Jardin[2], N.M. Ferraro[2] and B.C. Lyons[1]

[1] General Atomics, San Diego, CA, United States of America
[2] Princeton Plasma Physics Laboratory, Princeton, NJ, United States of America

E-mail: zhaoc@fusion.gat.com

Received 2 March 2024, revised 12 September 2024
Accepted for publication 27 September 2024
Published 8 October 2024

CrossMark

Abstract
The next generation of large tokamaks, including ITER, will be equipped with a disruption mitigation system (DMS) that can be activated if a disruption is deemed to be imminent. Introducing impurities by pellet (large or shattered) or massive gas injection has been shown to be an effective mitigation mechanism on many tokamaks. The goal of the mitigation is to lessen the thermal and electromagnetic loads from the disruption without generating enough high-energy (runaway) electrons to damage the device. Variations of this mitigation process with impurity injection are presently being tested on many experiments. We have modeled one such impurity injection experiment on DIII-D using the M3D-C1 nonlinear 3D extended MHD code (Jardin *et al* 2012 *Comput. Sci. Discovery* **6** 014002), The model includes an argon large pellet injection and ablation model, impurity ionization, recombination, and radiation, and runaway electron formation and subsequent evolution, including both Dreicer and avalanche sources. We obtain reasonable agreement with the experimental results for the timescale of the thermal and current quench and for the magnitude of the runaway electron plateau formed during the mitigation. This is the first 3D full MHD simulation with pellets and REs to simulate the disruption process and it also provides a partial validation of the M3D-C1 DMS model.

Keywords: runaway electron seeds, pellet injection, thermal quench, current quench, runaway electron plateau, M3D-C1 modeling

(Some figures may appear in colour only in the online journal)

1. Introduction

During a tokamak disruption, the plasma temperature and current drop abruptly and a population of high-energy runaway electrons (RE) can be formed which may later escape confinement and impact the tokamak walls. The RE current partially or totally replaces the current carried by the thermal particles and could sustain the plasma current during the latter part of the disruption current quench. This is known as a 'runaway electron plateau' [1, 2]. The ability to predict the formation and evolution of a RE population is important for the operation of existing experiments and the planning of future experiments.

Many present-day tokamaks have pellet injection systems that can be used to study the efficacy of disruption mitigation by massive impurity injection. The shattered pellet injection (SPI) is a common mitigation technique and is currently planned to be utilized on ITER. However, this process may generate RE which could cause substantial damage to the device. This is especially worrisome for the next generation of

* Author to whom any correspondence should be addressed.

tokamaks such as ITER that have large plasma current. Many experiments with impurity pellets are presently being carried out on DIII-D, JET, ASDEX-U, and other tokamaks to better understand the effectiveness of the pellet injection and its role in RE formation and RE-plasma interactions. Our goal is to model these experiments as realistically as possible to both validate our model and to aid in the interpretation of the experimental results.

The simulation model described here is multi-physics and multi-scale. It includes the physics of the ablation of the impurity pellet and its subsequent evolution, the ionization and radiation from the ablated material, the magnetohydrodynamics (MHD) of the background plasma, and the formation and evolution of the RE. The model is implemented through extensions of M3D-C1 [3], a massively parallel 3D MHD code which is run on high-performance computers. The simulated event includes both the pellet-induced thermal quench (TQ) and the subsequent current quench (CQ) with RE plateau formation.

In this paper, we present a full 3D MHD simulation of the DIII-D mitigated disruption shot 177043, with argon impurity pellet injection, including the RE sources and dynamics. This is a comprehensive multi-physics, multi-scale 3D simulation of a mitigated disruption experiment in a major tokamak, but does not include the resistive wall effect in the TQ which can also affect the RE generation during the TQ [4]. It provides a wealth of information regarding the details of the physical processes leading to the formation and subsequent loss of the RE beam. The 3D simulation results are in qualitative agreement with the experimentally measured plasma current and runaway losses vs time. However the simulation misses some of the high frequency MHD events due to the resolution limits, which causes the RE to be generated earlier in the TQ than in the experiment. In contrast, we find that a companion 2D simulation with the same RE source terms and plasma transport coefficients greatly over-estimates the magnitude of the final RE current plateau. This indicates that 3D effects are important, in particular for prompt RE loss. This adds credence to proposals to promote RE prompt loss by the addition of runaway electron mitigation coils (REMC).

This paper is organized as follows. In section 2 we introduce the 'fluid' RE model, with sources, and describe how it has been implemented in the M3D-C1 code. Section 3 describes the equations used for the impurity pellet and how they modify the bulk conservation equations. In section 4 we present a simulation of DIII-D shot 177043, with impurity pellet injection, including the RE sources and dynamics, and compare the simulation results with experimental data. In section 5, we compare the 3D simulation result to a companion 2D simulation to explain the importance of the 3D RE-plasma interaction during the disruption. Section 6 contains a discussion and conclusions from this work.

2. The RE model in M3D-C1

M3D-C1 is an initial value code which employs high-order C^1 continuous finite elements in 3 dimensions [3]. It has options for reduced MHD or full MHD, linear or non-linear, and cylindrical or toroidal geometry. In our RE model, we treat the runaway electrons as a fluid species which interacts with the MHD background plasma [2, 5, 6]. The runaway electrons interact with the bulk plasma through the runaway current which is denoted by $\mathbf{J}_{\mathrm{RA}}$ and is described by

$$\mathbf{J}_{\mathrm{RA}} = -en_{\mathrm{r}}\left(c\frac{\mathbf{B}}{B} + \frac{\mathbf{E}\times\mathbf{B}}{B^2}\right). \quad (1)$$

Here n_{r} is the RE density. Bold faced E and B are the electric and magnetic field, and c is the velocity of the runaway electrons, assumed to be the speed of light. We assume that the average kinetic energy of runaways is much smaller than the electromagnetic energy in this particular case, so that we ignore the magnetic drift and the relativistic anisotropic pressure. However, it is not a general fact that $\mathbf{E}\times\mathbf{B}$ drift of the RE is dominant in high energy RE beam cases.

For the runaway density time evolution, we use the following equation

$$\frac{\partial n_{\mathrm{r}}}{\partial t} + \nabla\cdot\left[n_{\mathrm{r}}\left(\frac{c\mathbf{B}}{B} + \mathbf{v}_{\perp}\right)\right] = \nabla\cdot(\mathbf{D_r}\cdot\nabla n_{\mathrm{r}}) + S_{\mathrm{RE}}. \quad (2)$$

Here S_{RE} is the source term for RE generation. The $\mathbf{v}_{\perp}$ term is the perpendicular drift velocity of the runaway electrons which is assumed to be equal to the bulk plasma $\mathbf{E}\times\mathbf{B}$ drift. $\mathbf{D_r} = D_{\mathrm{r}}\mathbf{BB}/B^2$ is a tensor parallel diffusion operator for the runaway electrons. In this paper we use the value of RE diffusivity $D_{\mathrm{r}} \sim 100\ \mathrm{m^2\,s^{-1}}$. This somewhat artificial number is about 100 times larger than the cross-field diffusion of the thermal electrons. This diffusion term is much smaller than the advection term (2nd term on the left). It's value does not affect the RE density very much but serves to smooth the numerical noise induced by the large advection term.

The runaway source consists of two mechanisms: Dreicer and avalanche [7, 8]. In this work, the avalanche source dominate the RE generation. However, we note here that the hot-tail source [9] has not been included in our modeling. This source would add to the Dreicer source, and so it is likely that we are underestimating the initial RE source during the TQ. This additional source term should be considered in future disruption simulations.

The Dreicer growth [7] occurs when the acceleration due to the electric field exceeds the collisional drag. The non-relativistic threshold electric field can be derived from the force balance of the electric field acceleration and the collisional drag. If there is no other loss mechanism, the electric field threshold of RE generation from an electron traveling at thermal velocity in a discharge with electron temperature T_{e} is given by equation (3)

$$E_{\mathrm{D}} = \frac{n_{\mathrm{e}}e^3\ln\Lambda}{4\pi\epsilon_0^2 T_{\mathrm{e}}}. \quad (3)$$

Here n_{e} is the thermal electron density and $\ln\Lambda$ is the Coulomb logarithm. Electrons with velocities larger than thermal will become runaways at lower fields. (Actually, the critical field as given in reference [7] is $0.43E_{\mathrm{D}}$.)

However, special relativity requires that the electron velocity cannot be larger than the speed of light $v < c$, and this gives a minimum E-field required to generate runaway electrons as equation (4)

$$E_{\mathrm{C}} = \frac{n_{\mathrm{e}} e^3 \ln\Lambda}{4\pi\epsilon_0^2 m_{\mathrm{e}} c^2} = \frac{T_{\mathrm{e}}}{m_{\mathrm{e}} c^2} E_{\mathrm{D}}. \tag{4}$$

In M3D-C1, we use the Connor–Hastie form for the relativistic Dreicer source term [8] as given in equation (5).

$$S_{\mathrm{D}} = n_{\mathrm{e}} \nu_{\mathrm{ee}} \epsilon_{\mathrm{D}}^{-\frac{3}{16}} \exp\left[-\frac{1}{4}\epsilon_{\mathrm{D}}^{-1} + (1 + Z_{\mathrm{eff}})^{\frac{1}{2}} \epsilon_{\mathrm{D}}^{-\frac{1}{2}}\right]. \tag{5}$$

Here $\nu_{\mathrm{ee}} = n_{\mathrm{e}} e^4 \ln\Lambda / (4\pi\epsilon_0^2 m_{\mathrm{e}}^2 v_{\mathrm{te}}^3)$ is the thermal electron–electron collision frequency, $v_{\mathrm{te}} = \sqrt{2T_{\mathrm{e}}/m_{\mathrm{e}}}$ is the thermal electron velocity, $\epsilon_{\mathrm{D}} = E_{||}/E_{\mathrm{D}}$ is the ratio of the parallel electric field to the Dreicer field and Z_{eff} is the effective nuclear charge.

In the present paper, we use the Connor–Hastie model for the Dreicer effect, assuming that the additional mechanisms such as deviation of threshold electric field E_{C} [10–12] and phase space diffusion due to kinetic instabilities [13, 14] are negligible.

After the Dreicer seeds provides the first batch of runaway electrons, and when there are sufficient RE at the end of the thermal quench, the avalanche or 'knock-on' mechanism dominates the RE generation.

For the avalanche source, we use the Rosenbluth–Putvinski model [15] as given in equation (6)

$$S_{\mathrm{A}} = n_{\mathrm{r}} \nu_{\mathrm{c}} \frac{\epsilon_{\mathrm{C}} - 1}{\ln\Lambda} \sqrt{\frac{\pi\zeta}{3(Z_{\mathrm{eff}} + 5)}} \exp\left[1 - \epsilon_{\mathrm{C}}^{-1} + \frac{4\pi (Z_{\mathrm{eff}} + 1)}{3\zeta (Z_{\mathrm{eff}} + 5)(\epsilon_{\mathrm{C}}^2 + 4\zeta^{-2} - 1)}\right]. \tag{6}$$

Here $\epsilon_{\mathrm{C}} = E_{||}/E_{\mathrm{C}}$ is the ratio of the parallel electric field to the critical field, and $\nu_{\mathrm{c}} = n_{\mathrm{e}} e^4 \ln\Lambda / (4\pi\epsilon_0^2 m_{\mathrm{e}}^2 c^3) = \nu_{\mathrm{ee}} v_{\mathrm{te}}^3 / c^3$ is treated as the RE-electron collision frequency. The ζ factor represents the collision effect averaging along the electron trajectory, which is sensitive to the geometry of the fusion device, and exhibits interesting physics in different geometries. In this work, we focus on the geometry similar to typical tokamaks like DIII-D and use the tokamak assumption of the ζ factor as $\zeta \approx [1 + 1.46\sqrt{(r/R)} + 1.72(r/R)]^{-1}$ [18], where r is the minor radius and R is the major radius. However, other factors, such as collisions between RE and bound electrons, synchrotron radiation damping, magnetic field fluctuations, and the collisional effects of high-Z impurities, also influence the secondary REs. A comprehensive understanding of these effects requires kinetic modeling. These are outside the scope of our current study and are not included in the simulation in this paper.

We also use the zero resistivity assumption for the RE current, so that the runaways do not contribute to the parallel electric field and Ohmic-heating. The MHD equations in the presence of runaways are then given in equations (7)–(11)

$$\frac{\partial n}{\partial t} + \nabla \cdot (n\mathbf{v}) = \nabla D \nabla n. \tag{7}$$

$$n m_{\mathrm{i}} \frac{\mathrm{d}\mathbf{V}}{\mathrm{d}t} = (\mathbf{J} - \mathbf{J}_{\mathrm{RA}}) \times \mathbf{B} - \nabla p - \nabla \cdot \Pi_i, \tag{8}$$

$$\mathbf{E} = -\mathbf{V} \times \mathbf{B} + \eta (\mathbf{J} - \mathbf{J}_{\mathrm{RA}}), \tag{9}$$

$$\frac{\partial \mathbf{B}}{\partial t} = -\nabla \times \mathbf{E}, \tag{10}$$

$$\frac{n}{(\gamma - 1)}\left[\frac{\partial T_{\mathrm{e}}}{\partial t} + \nabla \cdot (T_{\mathrm{e}} \mathbf{V})\right] = -n T_{\mathrm{e}} \nabla \cdot \mathbf{V} - \boldsymbol{\nabla} \cdot \mathbf{q_e} + \mathbf{Q_e} + \Pi_e : \nabla \mathbf{V} + \eta (\mathbf{J} - \mathbf{J}_{\mathrm{RA}})^2. \tag{11}$$

Equation (7) is the bulk plasma density equation. Here D is the (small) density diffusion coefficient required for numerical stability. Equation (8) is the momentum equation where $\mathbf{V}$ is the flow velocity, and $\mathbf{J}$ is the total current. Equations (9) and (10) are the electromagnetic field equations with runaway current. Here η is the bulk plasma Spitzer resistivity. We subtract the runaway current from the total current in the electric field equation since it is assumed to be collisionless. Equation (11) is the electron temperature equation, where $\mathbf{q_e} = -(\kappa_\perp \nabla_\perp + \kappa_{||} \nabla_{||}) \cdot (T_{\mathrm{e}})$ is the electron heat flux, $\kappa_\perp$, $\kappa_{||}$ are the thermal conductivities perpendicular and parallel to the magnetic field. $\mathbf{Q_e}$ is the heating source from the ionization, radiation and the ion-electron collision transfer. Π_{e} is the electron viscosity. We have subtracted the runaway current from the ohmic heating term (last term on the right) of equation (11).

3. 3D pellet model in M3D-C1

We have also implemented a pellet injection and ablation model into the M3D-C1 code. A pellet is defined with an initial position in cylindrical coordinates $(R, \phi, Z) = (R_{\mathrm{p}}, \phi_{\mathrm{p}}, Z_{\mathrm{p}})$, initial velocity (v_R, v_ϕ, v_Z), and initial radius r_{p}. As the pellet moves ballistically through the plasma, it ablates according to one of several models. In this paper, for the pellet, we use the ablation rate given by reference [16–18] which is a function of r_{p} and the background plasma's electron density and temperature. As the pellet shrinks, the ablated impurities are deposited as neutrals in the M3D-C1 simulation domain. The deposition cloud is a 3D density source defined as a Gaussian distribution in the poloidal plane and a simplified (0-order of Bessel function I_0) von Mises distribution in the toroidal angle:

$$S_z = G_{2\mathrm{D}} \exp\left[\frac{\cos(\phi - \phi_{\mathrm{p}})}{V_{\mathrm{t}}^2}\right] \tag{12}$$

where $G_{2\mathrm{D}} = (2\pi R V_{\mathrm{p}}^2)^{-1} \exp[-((R - R_{\mathrm{P}})^2 + (Z - Z_{\mathrm{p}})^2)/2V_{\mathrm{p}}^2]$. Here V_{p} and V_{t} are the poloidal and toroidal half-widths taken to be $V_{\mathrm{p}} = 0.05$ m and $V_{\mathrm{t}} = 0.4\pi$ in radiance. These relatively large distribution widths are set by numerical resolution requirements and likely miss some radiative cooling and RE generation localized near the pellet.

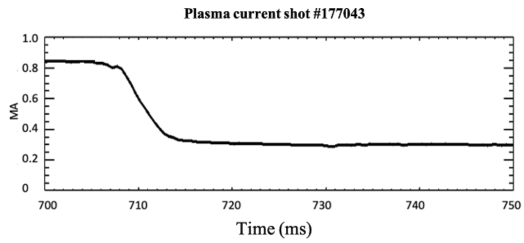

Figure 1. 177043 traces of the plasma current from 700 ms to 750 ms.

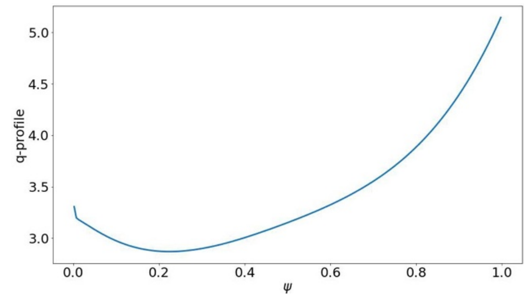

Figure 2. DIII-D q-profile using in M3D-C^1 modeling.

This deposition model should be improved in future simulations. The continuity equation for each impurity charge state is

$$\frac{\partial n_z}{\partial t} + \nabla \cdot (n_z \mathbf{V}) = \nabla \cdot (D_z \cdot \nabla n_z) + \sigma_z, \tag{13}$$

with the source $\sigma_z = \mathcal{I}_{z-1} n_{z-1} - (\mathcal{I}_z + \mathcal{R}_z) n_z + \mathcal{R}_{z+1} n_{z+1} + S_z$, where $\mathcal{I}_z$ is the ionization rate from charge state z to $z+1$, $\mathcal{R}_z$ is the recombination rate from z to $z-1$, and S_z is the external source from the pellet ablation, which is only non-zero for $z = 0$.

With impurities included, the equation (8) yields to equation (14) and the ion temperature equation with impurities is as given in equation (15). The electron temperature equation still remains the same as equation (11) for the two-temperature calculation with impurity pellets

$$(n_\mathrm{i} m_\mathrm{i} + \Sigma n_z m_z) \frac{\mathrm{d}\mathbf{V}}{\mathrm{d}t} = (\mathbf{J} - \mathbf{J}_\mathrm{RA}) \times \mathbf{B} - \nabla p - \nabla \cdot \Pi + \varpi \mathbf{V}, \tag{14}$$

$$\frac{n_*}{(\gamma - 1)} \left[\frac{\partial T_\mathrm{i}}{\partial t} + \nabla \cdot (T_\mathrm{i} \mathbf{V}) \right] + \sigma_* T_\mathrm{i} = -n T_\mathrm{i} \nabla \cdot \mathbf{V} - \boldsymbol{\nabla} \cdot \mathbf{q}_* + \mathbf{Q}_* + \Pi_* : \nabla \mathbf{V} + \frac{1}{2} \varpi V^2. \tag{15}$$

Here the subscript $*$ denotes a sum over the bulk ion and all impurity charge states for the density, heat flux, heating source/sink and viscosity. $\varpi = \Sigma m_z \sigma_z$ is the mass of all the impurity sources. The ionization and recombination rates, $\mathcal{I}_z$ and $\mathcal{R}_z$, and line-radiation power (included in Q_z) are calculated from a coronal, non-equilibrium model based on ADPAK atomic data as used in the KPRAD code [16]. More details for this impurity model can be found in [17, 18]. With equations (14) and (15) implemented in the code, we can model the entire disruption process with pellet injection and RE current generation, starting with an experimental equilibrium.

4. Simulation of DIII-D shot 177043

We have carried out a 3D full MHD simulation of a mitigated disruption in DIII-D shot 177043, in which an argon pellet is injected at time $t = 705$ ms. This shot produced a thermal quench and subsequent current quench which exhibited a RE plateau after $t = 715$ ms as shown in figure 1.

The initial equilibrium (as $t = 0$ ms in the simulation) for the M3D-C1 modeling was taken from an EFIT geqdsk file for shot 177043 at time 705 ms. The argon pellet was modeled with an initial position of $R = 2.11$ m, $Z = 0.53$ m, with initial radius 3 mm and velocity $|v_\mathrm{pr}| = 150$ m s^{-1}, $|v_\mathrm{p}z| = 130$ m s^{-1} and pellet density of 2.5×10^{28} m^{-3}.

Figure 2 is the experimental safety factor q as a function of the normalized minor radius. Note that there is a reversed shear region with a minimum at $(r/a) = 0.2$ where $q = 3$. This location is especially suseptical to MHD instabilities. The pre-injection electron density is 3×10^{19} m^{-3}. The transport coefficients used in the M3D-C1 code are shown in the appendix. The plasma resistivity used is Spitzer.

Figure 3 shows the experimental plasma current as well as the average temperature, the total plasma current, and the RE current as functions of time in the M3D-C1 simulation. Shortly after the pellet enters the plasma, the temperature drops near the pellet from 0.0 ms to 1.8 ms, but the core temperature remains at the same level, which is the so called pre-TQ phase. The decreasing temperature near the pellet leads to an increasing resistivity, which produces a large parallel electric field from $E_{||} = \eta J_{||}$, since η increases faster than $J_{||}$ decreases. This provide an $E_{||}$ larger than E_C during the pre-TQ phase, and produces runaway electrons through the Dreicer source term, equation (5). After that the avalanche and Dreicer source are both generating REs. When the pellet reaches the core, the core temperature rapidly drops starting from about 1.8 ms which is the start of the TQ (1.8 ms–3.0 ms). During the TQ phase, runaways are being generated but are also being lost due to MHD activity and the destruction of surfaces, so the RE current can decrease or increase during the TQ. Because our simulation exhibited less MHD activity that the experiment, there was only a small drop in RE current at $t = 2.5$ ms. Then the losses and MHD-runaways interactions cause the RE current to decrease at about 4.0 ms in the early current quench phase.

During the early CQ ($t = 3.0$ ms–5.5 ms), the RE-MHD interaction also destroys magnetic surfaces so that the average temperature drops due to parallel transport along the stochastic field lines. The runaway losses exceed the sources in the period from 4.0 to 6.0 ms during the early current quench phase, and then reach a balance producing a runaway current nearly constant but still oscillating in time from 6.0 ms to 12.0 ms. At $t = 10.0$ ms the total plasma current is almost entirely carried by the runaway electrons. The simulation value of 0.3 MA is similar to the experimental result. A RE plateau is formed, but

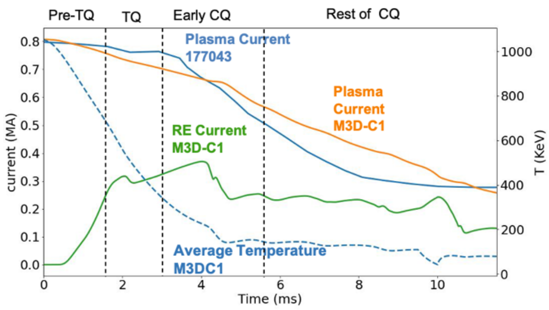

Figure 3. Time history of the plasma current from the experiment and the average temperature, total plasma current and the RE current in M3D-C1 simulation.

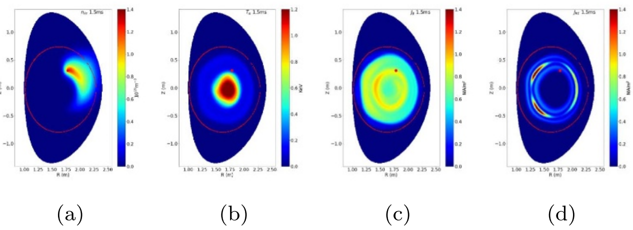

Figure 4. 2D structure (in the injection plane) of (*a*) argon density, (*b*) electron temperature, (*c*) plasma current and (*d*) runaway current at $t = 1.5$ ms in the simulation.

it exhibits some oscillation in time. This is discussed further in the following.

We next present a series of more detailed diagnostic plots from the simulation. We note that these detailed diagnostic images do not in general exist for the experimental data, but are useful for increasing our understanding of the physical processes being modeled in the simulation.

4.1. Numerical results in the pre-TQ phase (0.0 ms–1.8 ms)

Figures 4 and 5 show the ablated argon impurity density, electron temperature, plasma current, runaway current, Poincare plot and the q-profile at $t = 1.5$ ms in the pre-TQ phase. The red circle line is the last closed surface and the red dot is the center of the argon pellet. In the pre-TQ phase, the argon impurities begin to diffuse along the magnetic field lines as the pellet is moving on its trajectory towards the magnetic axis as shown in figure 4(*a*). The radiation from the impurity cools the plasma from the edge to the center as it moves inward as shown in figure 4(*b*). This cooling of the periphery leads to a steepened pressure profile which forms a current sheet in the steep pressure gradient region as shown in figure 4(*c*). The current sheet excites MHD instabilities (mainly 3/1 mode) as shown in figure 5(*a*). This reduces the q-profile near the island region as shown in figure 5(*b*). The 3/1 island shown in the Poincare plot figure 5(*a*) confines the REs interior to it as shown in figure 4(*d*).

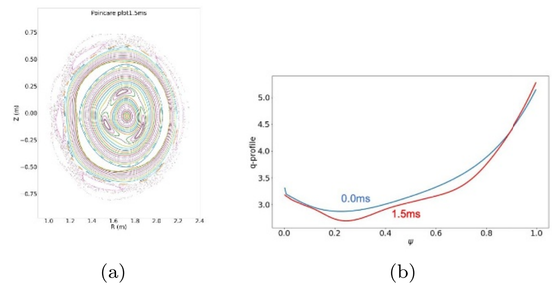

Figure 5. (*a*) Poincare plot and (*b*) q-profile at $t = 1.5$ ms in the pre-TQ phase.

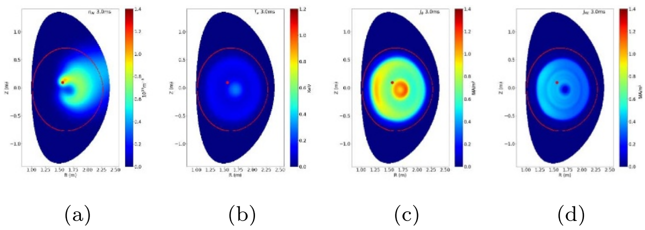

Figure 6. 2D structure of (*a*) argon density, (*b*) electron temperature, (*c*) plasma current and (*d*) runaway current at $t = 3.0$ ms in the simulation.

4.2. Numerical results in the TQ phase (1.8 ms–3.0 ms)

Figures 6 and 7 show the ablated argon impurity density, electron temperature, plasma current, runaway current, Poincare plot and the q-profile at $t = 3.0$ ms in the TQ phase. In the TQ phase, the argon impurity reaches the core plasma region as shown in figure 6(*a*) and it reduces the core temperature quickly as shown in figure 6(*b*). The 3/1 magnetic islands induced during the pre-TQ phase keeps growing during the TQ as shown in figure 7(*a*). The growing island squeezes the plasma current into the center as shown in figure 6(*c*). The squeezed plasma current in the core reduces the central q-profile to under $q = 2$ as shown in figure 7(*b*). The 3/1 islands induced in the pre-TQ phase near the core also disappears because of this effect as is shown in figure 7(*a*). At this time the RE distribution becomes uniform throughout the core, as shown in figure 6(*d*) because the avalanche source dominates the RE generation and closed surfaces are able to confine the REs.

4.3. Numerical results in early CQ time (3.0 ms–5.5 ms)

Figures 8 and 9 show the ablated argon impurity density, electron temperature, plasma current, runaway current, Poincare plot and the q-profile at $t = 5.0$ ms at the early-CQ time.

At the early CQ time, the pellet already has passed the core region and the impurities have diffused throughout the whole plasma region as shown in figure 8(*a*). The MHD modes induced during the TQ time cause the magnetic islands size to keep growing so that the magnetic islands overlap with each other, which causes stochastic magnetic fields as shown in

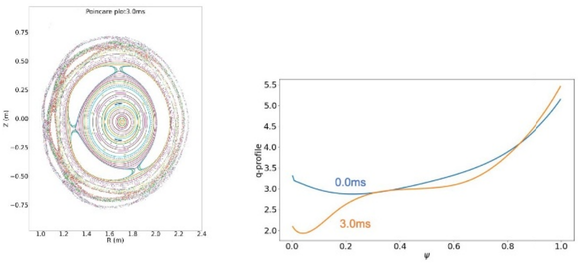

(a) (b)

Figure 7. (*a*) Poincare plot and (*b*) q-profile at $t = 3.0$ ms in the TQ phase.

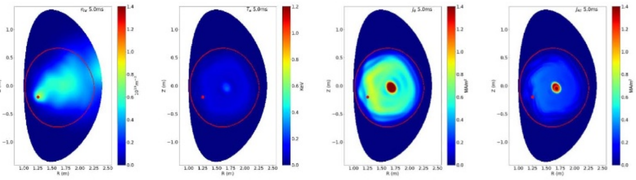

(a) (b) (c) (d)

Figure 8. 2D structure of (*a*) argon density, (*b*) electron temperature, (*c*) plasma current and (*d*) runaway current at $t = 5.0$ ms in the simulation.

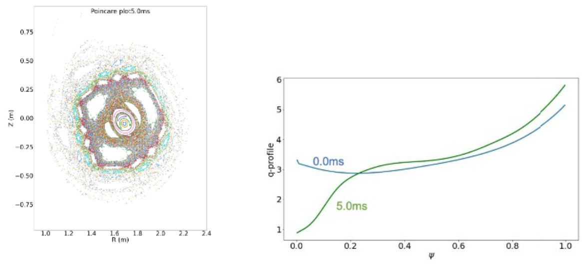

(a) (b)

Figure 9. (*a*) Poincare plot and (*b*) q-profile at $t = 5.0$ ms in the early CQ phase.

figure 9(*a*). The destroyed magnetic surfaces could not confine the heat or the REs at this time. Both the electron temperature and RE current decrease in the stochastic field region as shown in figures 8(*b*) and (*d*). There is still a small region in the plasma core which has closed field lines, so that the RE current is confined inside that region as shown in figures 8(*c*) and (*d*).

4.4. Numerical results in the rest of CQ time (5.5 ms–12.0 ms)

After the early CQ time, the argon impurities cover the whole plasma region uniformly as shown in figure 10(*a*). The temperature remains at a low value during the rest of the CQ time as shown in figure 10(*b*).

The runaway current during the rest of the CQ time is not always constant in time but is oscillating around a constant value. This is because of the 3D RE-MHD interactions during this time and is different from the regular RE plateau results presented in previous simulations [15].

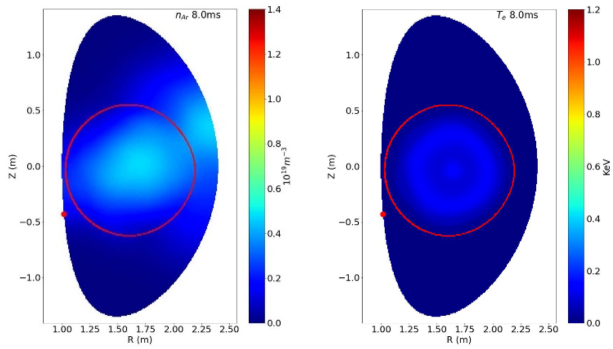

(a) (b)

Figure 10. 2D structure of (*a*) argon density, (*b*) electron temperature $t = 8.0$ ms in the simulation.

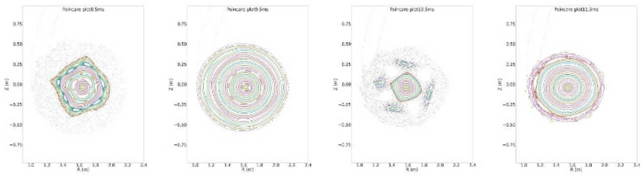

(a) (b) (c) (d)

Figure 11. Poincare plot at (*a*) 8.5 ms, (*b*) 9.5 ms, (*c*) 10.5 ms (*d*) 11.5 ms.

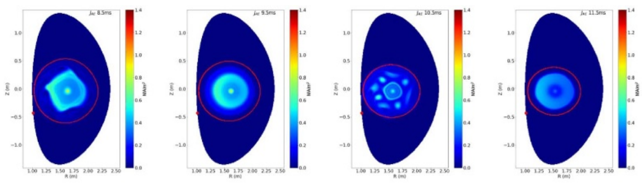

(a) (b) (c) (d)

Figure 12. Runaway current density at (*a*) 8.5 ms, (*b*) 9.5 ms, (*c*) 10.5 ms and (*d*) 11.5 ms.

Figures 11 and 12 show the Poincare plots and RE current density from 8.5 ms to 11.5 ms which contains a whole period of the RE current oscillation. At that time the plasma current is mostly carried by the runaways and the interactions between RE and MHD modes are stronger than the time just after the early CQ (5.5 ms–8.5 ms). We next explain the physical processes leading to the current oscillation during this period.

When the MHD modes form magnetic islands and destroy the closed flux surfaces near the islands as shown in figure 11(*a*), the runaway current is localized inside the islands and is lost in the stochastic field area as shown in figure 12(*a*). The runaways inside the islands interact with the modes and stabilize the MHD instabilities. With the modes stabilized, the magnetic surfaces are reformed and the islands disappear as shown in figure 11(*b*). Then the runaway current grows inside the closed magnetic surfaces as shown in figure 12(*b*). When the RE current increases, the MHD modes become unstable again, and form magnetic islands that destroy the

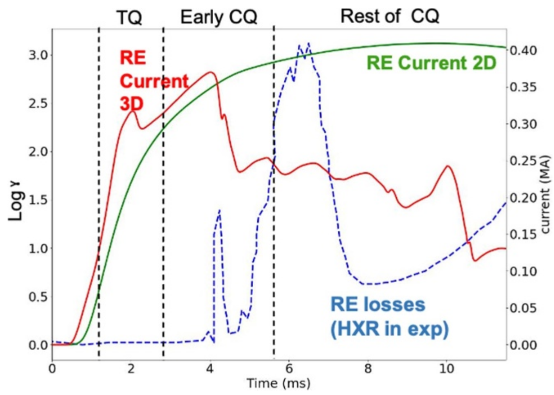

Figure 13. 2D and 3D runaway current simulation results and hard x-ray signal with the unit as normalized intensity in experiment.

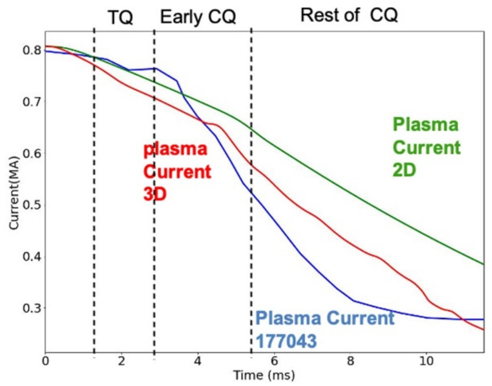

Figure 14. Plasma current of 2D, 3D simulation and experiment.

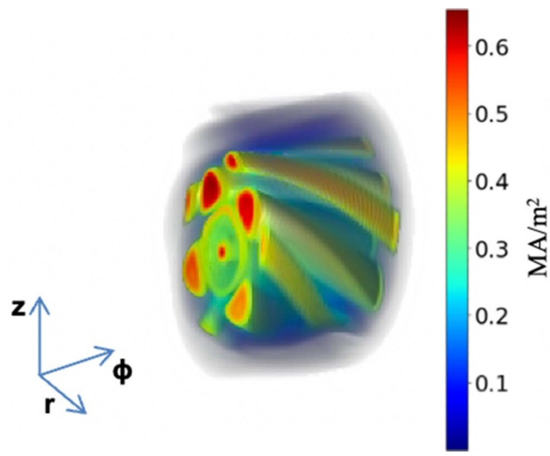

Figure 15. 3D runaway current filaments at $t = 11.0$ ms.

magnetic surfaces again as shown in figure 11(c). The magnetic islands again confine the REs inside the islands as shown in figure 12(c) and the modes are stabilized by the RE-MHD interactions. Then the islands disappear again and the RE current increases inside the closed surfaces as shown in figures 11(d) and 12(d). This periodic process repeats during the CQ from $t = 6.0$ ms to $t = 12.0$ ms and causes the RE current to fluctuate with time during the CQ.

5. Importance of 3D RE-MHD interactions during the disruption

We have also carried out a 2D simulation with the same initial equilibrium and transport coefficients as used in the 3D simulation to illustrate the importance of the 3D effects during the disruption with RE and impurities. Figure 13 shows the 2D and 3D RE current simulation results and the RE loss (hard x-ray signal) in the experiment. There is no RE loss in the 2D simulation but there is clear RE loss in the TQ and early CQ phases in both the experiment and 3D simulation. In the simulations, the REs are generated during the TQ both in the 2D and the 3D simulations but not in the experiment. The REs generated during the TQ are initially due to the parallel electric field $E/E_{\mathrm{D}} < 0.03$ as shown in figure 16 by Dreicer seed. We believe these seed electrons were also formed in the experiment, but were subsequently lost due to enhanced MHD activity, present in the experiment but not in the simulations. The high frequency MHD activities during the TQ were not well reproduced in the simulation, likely because of inadequate resolution. This will be the subject of further study.

During the CQ, we believe that the RE loss rate should be changing in time if there are MHD modes as shown in figure 13. There are also small perturbations in the experimental RE loss rate, but not as much as in the simulation at the same time.

The transport coefficients used in the simulation differ from those in the actual experiment and so we cannot expect detailed agreement in the results. Also, the sheared toroidal rotation and kinetic effects are not present in our simulation. However, our 3D simulation shows how the RE-MHD interaction can lead to oscillations in the RE current, although the oscillations in our simulation were larger than those observed in the experiment.

Figure 14 shows the 2D and 3D simulated and the experimental plasma current vs time. The total plasma current in the 3D simulation is clearly much closer to the experimental current trace than is the 2D result, indicating that 3D effects are important, the RE loss due to MHD activity in particular. Other 3D effects of importance are the RE localization in the magnetic islands, which is consistent with recent experimental observations [19]. These RE filaments, as shown in figure 15, serve to stabilize the instabilities and lead to the reforming of magnetic surfaces as mentioned in previous sections. This is the first 3D nonlinear simulation which has clearly shown the 3D RE filament structure.

6. Conclusions and discussion

We have implemented a RE fluid model with Dreicer and avalanche sources coupled with the background plasma in the 3D, fully non-linear, finite beta MHD code M3D-C1. In this paper, we use the code to model a complete DIII-D mitigated disruption process including the argon impurity pellet injection,

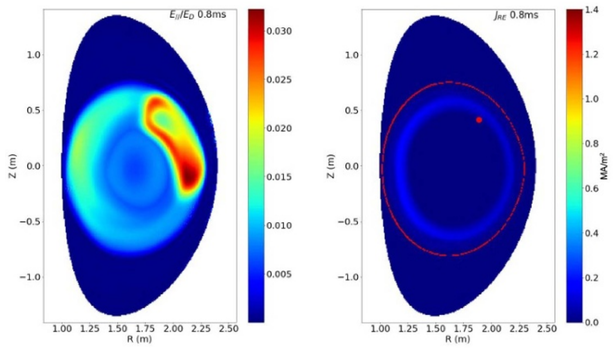

(a) (b)

Figure 16. 2D structure of (*a*) E/E_D, (*b*) runaway current density $t = 0.8$ ms in the simulation.

thermal quench, current quench, and the RE current plateau formation. This is the first 3D full MHD disruption simulation with impurity pellet and REs. The final total current value in the simulation is about 0.3 MA, almost all carried by RE, which is similar to the experimental results.

The modeling has produced a wealth of data concerning the evolution of the fields and currents, most of which is not possible to measure in experiments. The detailed results could not only explain some of the experimental results, but they also shed light on some interesting physics occurring in the complicated disruption processes.

The first one is that the 3/1 mode appears in the pre-TQ and TQ phase which produces the electro-magnetic field perturbations which destroy the closed magnetic surfaces and causes the RE loss. A deeper understanding of this process is still needed to help control the MHD instabilities induced during the TQ to maintain the closed surface and then reduce the RE loss to protect the devices.

The second one is that the MHD modes localize the REs inside the magnetic islands and form RE filaments. This is also the first time this has been found in a disruption simulation. The RE filaments could stabilize the MHD modes and restore the magnetic surfaces which help to confine the REs to form a RE plateau. Our 3D simulation data shows that the formation of the RE filaments significantly changes the RE loss rate during the CQ.

It is helpful to build a simulation database to design external coils (REMC) to generate MHD modes to control REs. By controlling the MHD activity through the REMC during the CQ, we may be able to control the RE filaments to get the ideal RE loss rate, leading to a larger RE plateau. This could potentially enable a 'soft landing' for a runaway discharge, allowing for better control and prevention of wall damage.

In our simulation, we find that the RE-MHD interactions are sensitive to the transport coefficients, a little bit higher transport coefficients would lower the amplitude of the MHD modes. And the RE loss rate does not linearly grow with the MHD amplitude. In a particular regime, the magnetic islands produced by the MHD events trap the RE inside the island and reduce the RE loss, but with stronger MHD activity, the RE loss rate increasing with higher MHD amplitude. It mainly depends on how the MHD modes destroy the surfaces. We will do more parameter scan simulations to reveal the relationships between RE loss rate and transport coefficients. Our present simulation predicts a short plasma current plateau (10.0 ms–12.0 ms) during the CQ as shown in figure 14, which is at a similar current value with the experiment and after 12.0 ms there's a discrepancy between our simulation and the experimental result. When the current is mostly carried by the REs, the runaway current keeps decreasing because of MHD instabilities. But in the experiments, the MHD modes are rarely induced during the RE plateau, and high frequency modes could interact with the REs, as could intrinsically kinetic modes [20]. These physical effects that are likely important in the experiments with RE plateau are not presently included in our simulations and cause discrepancies. This will be the subject of further study.

Acknowledgments

This material is based upon work supported by the U.S. Department of Energy, Office of Science, Office of Fusion Energy Sciences, using the DIII-D National Fusion Facility, a DOE Office of Science user facility, under Award(s) DE-FG02-95ER54309, DE-FC02-04ER54698, DE-SC0016452, DE-SC0018109 and DE-AC05-00OR22725.

Appendix

Transport coefficients	M3D-C1 unit	MKS
Density diffusion	6.5×10^{-7}	$1\ \mathrm{m^2\,s^{-1}}$
Perpendicular Viscosity	6.5×10^{-4}	$1000\ \mathrm{m^2\,s^{-1}}$
Compressional viscosity	6.5×10^{-3}	$10000\ \mathrm{m^2\,s^{-1}}$
Perpendicular thermal conductivity	1.3×10^{-6}	$2\ \mathrm{m^2\,s^{-1}}$
Parallel thermal conductivity	6.5	$1 \times 10^7\ \mathrm{m^2\,s^{-1}}$
Runaway current resistivity	0	0 Ohm·m

ORCID iDs

C. Zhao https://orcid.org/0000-0002-7351-6003
C. Liu https://orcid.org/0000-0002-6747-955X
S.C. Jardin https://orcid.org/0000-0001-6390-6908
N.M. Ferraro https://orcid.org/0000-0002-6348-7827
B.C. Lyons https://orcid.org/0000-0003-3232-1581

References

[1] Gill R.D. 1993 Generation and loss of runaway electrons following disruptions in JET *Nucl. Fusion* **33** 1613
[2] Eidietis N.W., Commaux N., Hollmann E.M., Humphreys D.A., Jernigan T.C., Moyer R.A., Strait E.J., Van Zeeland M.A., Wesley J.C. and Yu J.H. 2012 Control of post-disruption runaway electron beams in DIII-D *Phys. Plasmas* **19** 056109
[3] Jardin S., Ferraro N., Breslau J. and Chen J. 2012 Multiple timescale calculations of sawteeth and other global macroscopic dynamics of tokamak plasmas *Comput. Sci. Discovery* **6** 014002
[4] Bandaru V., Hoelzl M., Bergström H., Artola F.J., Särkimäki K. and Lehnen M. (The JOREK Team) 2024 Assessment of runaway electron beam termination and impact in ITER *Nucl. Fusion* **64** 076053
[5] Liu C., Zhao C., Jardin S.C., Ferraro N.M., Paz-Soldan C., Liu Y. and Lyons B.C. 2021 Self-consistent simulation of resistive kink instabilities with runaway electrons *Plasma Phys. Control. Fusion* **63** 125031
[6] Zhao C., Liu C., Jardin S.C. and Ferraro N.M. 2020 Simulation of MHD instabilities with fluid runaway electron model in M3D-C1 *Nucl. Fusion* **60** 126017
[7] Dreicer H. 1959 Electron and ion runaway in a fully ionized gas. I *Phys. Rev.* **115** 238
[8] Connor J.W. and Hastie R.J. 1975 Relativistic limitations on runaway electrons *Nucl. Fusion* **15** 415
[9] Smith H.M. and Verwichte E. 2008 Hot tail runaway electron generation in tokamak disruptions *Phys. Plasmas* **15** 072502
[10] Granetz R.S., Esposito B., Kim J.H., Koslowski R., Lehnen M., Martin-Solis J.R., Paz-Soldan C., Rhee T., Wesley J.C. and Zeng L. (ITPA MHD Group) 2014 An ITPA joint experiment to study runaway electron generation and suppression *Phys. Plasmas* **21** 072506
[11] Paz-Soldan C. *et al* 2014 Structure and overstability of resistive modes with runaway electrons *Phys. Plasmas* **21** 022514
[12] Bandaru V., Hoelzl M., Artola F.J., Papp G. and Huijsmans G.T.A. 2019 Simulating the nonlinear interaction of relativistic electrons and tokamak plasma instabilities: implementation and validation of a fluid model *Phys. Rev.* E **99** 063317
[13] Stahl A., Hirvijoki E., Decker J., Embréus O. and Fülöp T. 2015 Effective critical electric field for runaway-electron generation *Phys. Rev. Lett.* **114** 115002
[14] Aleynikov P. and Breizman B.N. 2015 Theory of two threshold fields for relativistic runaway electrons *Phys. Rev. Lett.* **114** 155001
[15] Rosenbluth M.N. and Putvinski S.V. 1997 Theory for avalanche of runaway electrons in tokamaks *Nucl. Fusion* **37** 1355
[16] Whyte D.G. *et al* 1997 Energy balance, radiation and stability during rapid plasma termination via impurity pellet injections on DIII-D *Proc. 24th European Physical Society Conf. on Controlled Fusion and Plasma Physics (Berchtesgaden, Germany, 9–14 June 1997)* vol 21A p 1137
[17] Ferraro N.M., Lyons B.C., Kim C.C., Liu Y.Q. and Jardin S.C. 2019 3D two-temperature magnetohydrodynamic modeling of fast thermal quenches due to injected impurities in tokamaks *Nucl. Fusion* **59** 016001
[18] Parks P.B. 2017 A theoretical model for the penetration of a shattered-pellet debris plume *Theory and Simulation of Disruptions Workshop* pp 17–19
[19] Kostadinova E.G., Orlov D.M., Koepke S., Skiff F. and Austin M. 2023 Energetic electron transport in magnetic fields with island chains and stochastic regions *J. Plasma Phys* **89** 905890420
[20] Paz-Soldan C. *et al* 2019 Recent DIII-D advances in runaway electron measurement and model validation *Nucl. Fusion* **59** 066025